

# Numerical Modeling of Wave Processes in Layered Media in the Arctic Region

A. V. Favorskaya, I. B. Petrov, D. I. Petrov, and N. I. Khokhlov

*Moscow Institute of Physics and Technology, Moscow, Russia*

*e-mail: petrov@mipt.ru*

Received March 17, 2015

**Abstract**—The aim of this work is the numerical simulation of wave propagation in media with linear-elastic and acoustic layers as exemplified by the seismic prospecting problems in the Arctic region and the explosive impact on an iceberg. The complete system of equations describing the state of a linearly elastic body and the system of equations describing the acoustic field are solved. The grid-characteristic method is used to provide the contact and boundary conditions, including the contact condition between acoustic and linear-elastic layers, to be correctly described.

**Keywords:** grid-characteristic method, numerical modeling, Arctic shelf seismic prospecting, icebergs

**DOI:** 10.1134/S2070048216040074

## 1. INTRODUCTION

The problem of the exploration of the Russian Arctic shelf remains topical due to the necessity of developing and prospecting hydrocarbon fields. The Russian Arctic shelf contains eight hydrocarbon fields discovered since 1983 until 1992 that have approximate total reserves of  $2700000000 \text{ m}^3$ . Among them, there are five federally important objects: Leningradskoe and Rusanovskoe in the Kara Sea; as well as Ledovoe, Ludlovskoe, and Murmanskoe in the Barents Sea. The Prirazlomnaya ice-resistant oil-producing platform is built in the Pechora Sea to develop the Prirazlomnoye oil field and the possibility of gas recovery at the Shtokmanovskoe field (Barents Sea) is being developed. The earlier estimated oil and gas resources for these fields need to be specified [1]. A factor complicating the oil development in the Arctic seas is the permanent presence of ice, in particular, icebergs [2–5].

Oil prospecting under the conditions of the Arctic region has its particular features. For example, one of the layers that prospecting signals have to transit is the seawater [6, 7]; another layer contributing to the measured or calculated wave responses is the ice. In addition to seismic prospecting, electromagnetic prospecting can also be considered effective in the search for hydrocarbons (see the review on this topic in [8]).

## 2. PROBLEM STATEMENT

In the present work, the complete system of equations, which describes the state of a continuous linearly elastic medium, and the complete system of equations, which describes the acoustic field, are solved. The components of movement velocity  $\vec{v}$  and Cauchy's symmetric stress tensor  $\sigma$  in a linearly elastic medium are described by the following equation system [9, 10]:

$$\rho \mathbf{v}_t = (\nabla \cdot \sigma)^T, \quad (1)$$

$$\sigma_t = \lambda (\nabla \cdot \vec{v}) \mathbf{I} + \mu (\nabla \otimes \mathbf{v} + (\nabla \otimes \mathbf{v})^T). \quad (2)$$

For the numerical simulation of the seawater layer and oil-containing inclusions, we used the ideal liquid approximation [11] and solved the complete system containing the equations describing the acoustic field of pressure and the components of velocity  $\mathbf{v}$ :

$$\rho \mathbf{v}_t = -\nabla p, \quad (3)$$

$$p_t = -c^2 \rho (\nabla \cdot \mathbf{v}). \quad (4)$$

In Eqs. (1) and (2),  $\lambda$  and  $\mu$  are the Lamé parameters defining the properties of the elastic material;  $\rho$  is the density;  $\bar{a} \otimes \bar{b}$  is the tensor product of vectors  $\mathbf{a}$  and  $\mathbf{b}$ ;  $(\mathbf{a} \otimes \mathbf{b})^{ij} = a^i b^j$ ; and  $\mathbf{I}$  is a single second-rank tensor. In Eq. (4),  $c$  denotes the sonic velocity in an ideal liquid. The P-wave velocity in a linearly elastic medium can be found from the formula

$$c_p = \sqrt{(\lambda + 2\mu)/\rho}, \quad (5)$$

and the S-wave velocity is calculated according to the following expression:

$$c_s = \sqrt{\mu/\rho}. \quad (6)$$

The boundary conditions with the set velocity at the boundary and with the set internal force, as well as the mixed boundary conditions, full adhesion contact conditions, free sliding conditions, and contact between the liquid and solid body, are implemented. The damages (cracks) that appear are taken into account by using the Mises criterion [12].

### 3. GRID-CHARACTERISTIC METHOD

For numerically solving the equation systems (1), (2) and (3), (4), we used the grid-characteristic method on curvilinear structural grids [13] that allows us to construct the correct numerical algorithms for calculating the boundary points and points on the interfaces between two media having different Lamé parameters and (or) densities.

System (1) and (2) in the two-dimensional case can be presented in the following form:

$$\mathbf{q}_t + \mathbf{A}_1 \mathbf{q}_{x_1} + \mathbf{A}_2 \mathbf{q}_{x_2} = 0. \quad (7)$$

In Eq. (7), vector  $\mathbf{q}$  is the vector composed of two components of velocity and three components of the symmetric stress tensor:

$$\mathbf{q} \in \{v_1, v_2, \sigma_{11}, \sigma_{22}, \sigma_{12}\}^T.$$

First, the method of splitting on spatial coordinates was used; as a result, two one-dimensional systems are obtained:

$$\mathbf{q}_t + \mathbf{A}_j \mathbf{q}_{x_j} = 0. \quad (8)$$

Each of these systems is hyperbolic and possesses the full set of eigenvectors with real eigenvalues; therefore, each system can be transformed as follows:

$$\mathbf{q}_t + \mathbf{\Omega}_j^{-1} \mathbf{\Lambda}_j \mathbf{\Omega}_j \mathbf{q}_{x_j} = 0,$$

where matrix  $\mathbf{\Omega}_j^{-1}$  is the one composed of eigenvectors;  $\mathbf{\Lambda}_j$  is a diagonal matrix, whose elements are eigenvalues. For all coordinates, matrix  $\mathbf{\Lambda}$  is of the following form (index  $j$  is omitted below wherever possible):

$$\mathbf{\Lambda} = \text{diag}\{c_p, -c_p, c_s, -c_s, 0\}.$$

After replacement of variables  $\mathbf{w} = \mathbf{\Omega} \mathbf{q}$ , each of the systems described by Eq. (8) falls into five independent scalar transfer equations:

$$\mathbf{w}_t + \mathbf{\Lambda} \mathbf{w}_x = 0.$$

One-dimensional transfer equations are solved either by the method of characteristics or common finite-difference schemes. When all components are transposed, the solution itself is restored:

$$\mathbf{q}^{n+1} = \mathbf{\Omega}^{-1} \mathbf{w}^{n+1}.$$

In the used software, application of TVD-difference schemes of the second order of accuracy [14] and 15 different limiters [15] are implemented; in the calculations, we mainly used the superbee limiter [16] and grid-characteristic schemes of second–fourth orders of accuracy [13].

### 4. CONDITION OF CONTACT BETWEEN LIQUID AND SOLID BODY

Let the equation system (1) and (2) be solved in part  $a$  of the integration domain, and let the equation system (3) and (4) be solved in part  $b$  of the integration domain. Let us consider the condition of contact between them. In the three-dimensional case, system (1) and (2) has three outputs, whereas system (3)

and (4) has one output. Thus, in order to find all four outputs, the following conditions of contact should be satisfied:

$$p^{b,n+1} = -(\boldsymbol{\sigma}^{a,n+1} \cdot \mathbf{n}) \cdot \mathbf{n}, \quad (9)$$

$$\boldsymbol{\sigma}^{a,n+1} \cdot \mathbf{n} - (\boldsymbol{\sigma}^{a,n+1} \cdot \mathbf{n}) \cdot \mathbf{n} = 0, \quad (10)$$

$$\mathbf{v}^{a,n+1} \cdot \mathbf{n} = \mathbf{v}^{b,n+1} \cdot \mathbf{n}. \quad (11)$$

Condition (9) is equality between the normal component of surface density of the forces from a solid body and the pressure in ideal liquid; condition (10) provides the tangential component of the surface density of forces from a solid body to be zero; and condition (11) sets the equality between normal components of the velocities in the ideal liquid and solid body. In (9)–(11),  $\mathbf{n}$  denotes the external normal to the solid body (and also the internal normal to the liquid).

Velocity vector  $\mathbf{V}$  is calculated in such a way that conditions (9)–(11) are satisfied. Then, we use the boundary condition with the set velocity for a solid body and the boundary condition with the set normal component of velocity for a liquid.

## 5. SEISMIC PROSPECTING ON THE ARCTIC SHELF

We carried out numerical experiments to solve the problems related to seismic prospecting under the conditions of the Arctic shelf. In all the calculations, the spatial step was 0.2 m; the time step was  $3 \times 10^{-5}$  s, and the total number of time steps was 15000. The considered ice layer was 4 m thick and  $917 \text{ kg/m}^3$  in density. The  $P$ - and  $S$ -wave velocities were assumed to be 3940 and 3650 m/s, respectively. The considered water layer was 100 m thick, which fits the sea depth at the Leningradskoe and Rusanovskoe fields in the Kara Sea [1]. The  $P$ - and  $S$ -wave velocities in the sediment (beneath the bottom) were 6500 and 3700 m/s, respectively; the sediment density was assumed to be  $2500 \text{ kg/m}^3$ . The water density was  $1000 \text{ kg/m}^3$ ; and the sonic velocity was 1500 m/s. The width of the integration domain was 1200 m. Then we calculated the bottom layer 600 m deep, with nonreflecting boundary conditions on its sides [10].

We considered the sources installed on the ice, within the ice, in the water beneath the ice, on the sea floor, and in the water without ice on the water surface. In all cases, the effect was simulated by the Ricker wavelet. Based on the results of the numerical experiments, a similarity was revealed for (a) the wave patterns when the sources are installed on the ice, within the ice, and in the water beneath the ice, (b) the reflections that appear, and (c) all types of seismograms (from surface- and seafloor-based receivers, with horizontal and vertical components of velocity, and with a velocity modulus). In addition, when the sources were installed on the seafloor, the presence of ice did not significantly affected the seismograms obtained on both the seafloor and the ice/water surface.

The receivers were installed on either the seafloor or the ice surface (in its presence); in the absence of ice, the receivers were on the water surface. If the receivers were installed on the seafloor, the locations of the sources were not important. The receivers at the bottom always provide more information: both vertical and horizontal components of velocity. In contrast, when the receivers are installed on either the ice or water surface, the horizontal component of velocity is lost. If the receivers are installed on ice, the construction of seismograms on the velocity modulus yields less information than the direct construction of seismograms on the vertical component of velocity due to the increase in amplitude as a result of the increment of the horizontal component, which carries no information. In addition, at the same intensity of the wave effect, the signals recorded by ice-based receivers are much weaker than those recorded by bottom receivers.

We considered four types of reservoirs at a depth of 50 m: short fluid-saturated, short averaged, elongated fluid-saturated, and elongated averaged. An elongated reservoir 20-m-thick was located over the entire width of the integration domain; thus, the nonreflecting boundary conditions were also set in its sides. The short reservoir was 20 m thick and 200 m long and wide. In the fluid-saturated reservoir, system (3) and (4) was solved at a density of  $900 \text{ kg/m}^3$  and sonic velocity of 1470 m/s. In the averaged reservoir, system (1) and (2) was solved with the following elastic characteristics:  $P$ - and  $S$ -wave velocities of 4000 and 1250 m/s, respectively and density of  $2000 \text{ kg/m}^3$ . The source was installed on ice.

Figure 1 presents wave patterns corresponding to all the mentioned reservoir types at time 0.135 s. Figure 2 shows the seismograms in the case of receivers installed on ice to measure the vertical component of velocity. Figures 1a and 2a illustrate the calculation results for the elongated fluid-saturated reservoir; Figs. 1b and 2b, the elongated averaged; Figs. 1c and 2c, the short fluid-saturated; and Figs. 1d and 2d,

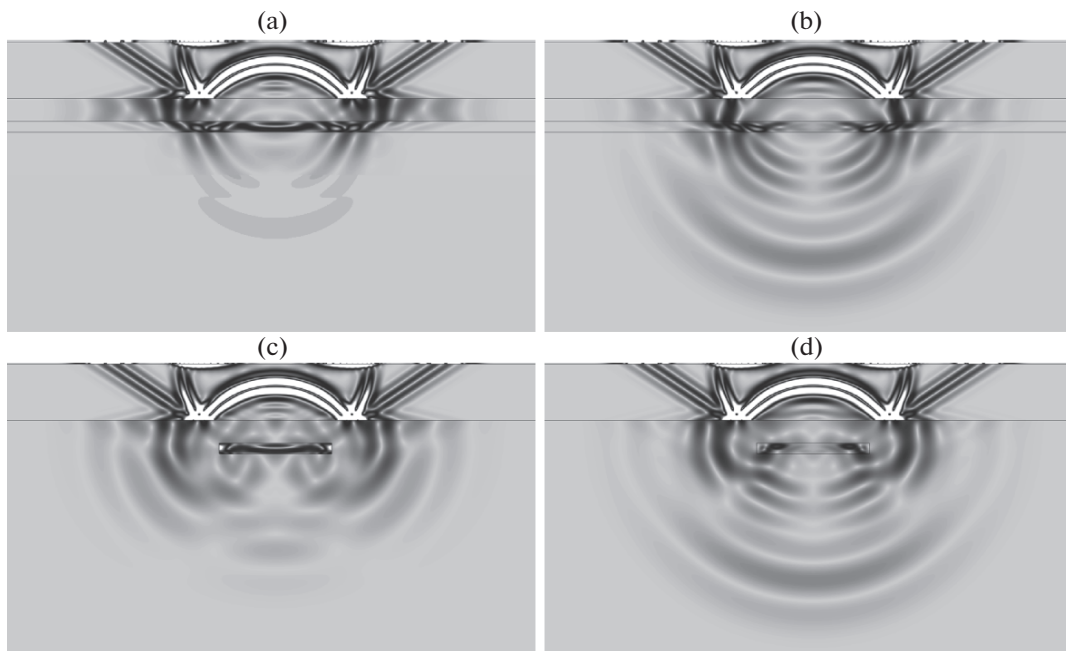


Fig. 1. Wave patterns. Reservoir types.

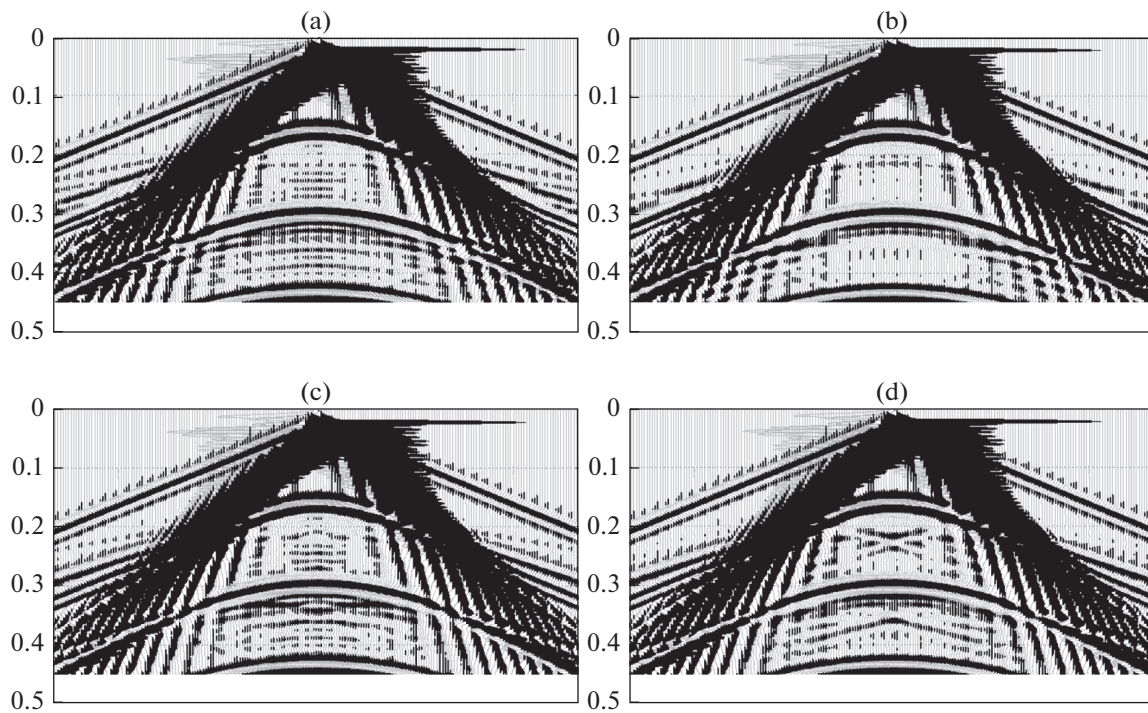
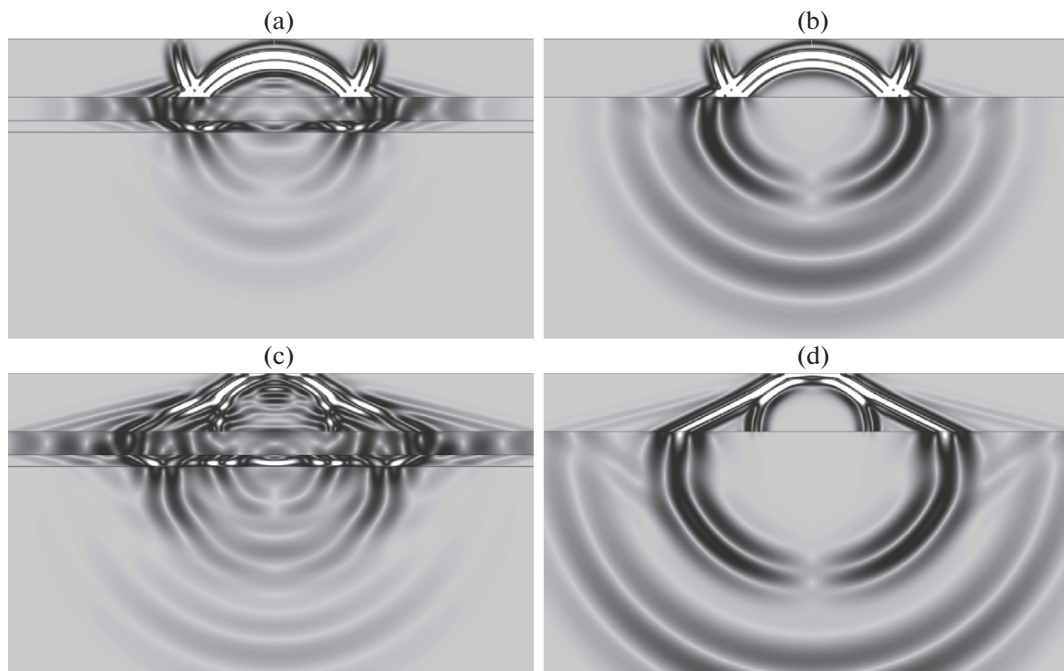


Fig. 2. Seismograms (vertical component of velocity). Reservoir types.

the short averaged. The seismograms in Fig. 2 and below are constructed by using the software described in [17].

In fluid-saturated reservoirs (Figs. 1a, 1c), we can see more intensive reflections than in the averaged reservoirs (Figs. 1b, 1d). The signals from fluid-saturated reservoirs are also more distinct. In all the seis-



**Fig. 3.** Wave patterns. Comparison between sources' locations in water (near its surface) and on the bottom. The case in the absence of ice.

mograms, for the cases of both bottom and ice-based receivers, the signals from fluid-saturated reservoirs are more distinct. In the figures below, the elongated fluid-saturated reservoir is considered.

Let us compare the wave patterns appearing when the source is installed in water near the surface and on the bottom without ice. Figure 3 depicts the wave reflections for these cases, and Fig. 4 shows the seismograms obtained from the receivers located on the water surface when measuring the vertical component of velocity. Figures 3a and 4a present the case with the source in the water near the surface; Figs. 3b and 4b, the same without reservoir; Figs. 3c and 4d, the case with the receiver on the bottom layer; Figs. 3d and 4d, the same without the reservoir. The wave patterns in Figs. 3a and 3b are present at time moment 0.135 s, while those in Figs. 3c and 3d are for time moment 0.09 s.

Let us compare the wave patterns appearing when the source is installed on the bottom in the presence of ice. Figure 5 shows the wave signals for these cases, while Fig. 6 presents seismograms obtained from ice-based receivers when measuring the vertical component of velocity. Figures 5a and 6a illustrate the case with an ice-based source; Figs. 5b and 6b, the same without a reservoir; Figs. 5c and 6c, the case with the source on the bottom; Figs. 5d and 6d, the same without a reservoir. The wave pattern in Figs. 5a and 5b are for time moment 0.135 s; those in Figs. 5c and 5d, for 0.09 s.

The velocity modulus is shown in Figs. 1, 3, and 5 in gray. We can see that the case of the source being installed on the bottom, even when the receivers are installed on the surface, provides more information in both the presence and absence of ice (in this case, the ice does not significantly affect the received signals). In contrast, if the source and receivers are located near the water surface in the absence of ice, the signal carries more information.

## 6. IMPACT EFFECT ON ICEBERG

We considered an iceberg measuring  $100 \times 200$  m with density  $917 \text{ kg/m}^3$ ; the  $P$ - and  $S$ -wave velocities were 3940 and 3650 m/s, respectively. The maximal value of the stress tensor in the Mises criterion [12] was assumed to be 1.2 MPa for the ice. Around the ice, we considered the water layer having a density of  $900 \text{ kg/m}^3$  and sonic velocity of 1470 m/s. We set the boundary condition of the free boundary at the upper boundary of the water and at the ice boundary not in contact with the water. Nonreflecting boundary conditions were set [10] on all sides of the integration domain. A surface force density of 0.9 in amplitude acted on the upper surface of the iceberg. The time step was  $2.5 \times 10^{-5}$  s and the spatial step was 0.1 m.

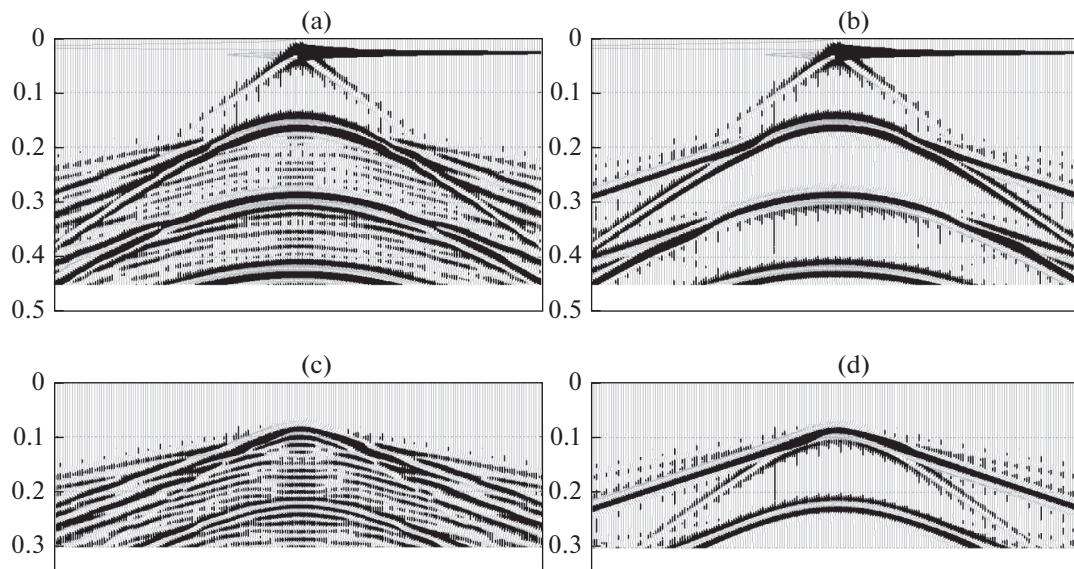


**Fig. 4.** Seismograms (vertical component of velocity). Comparison between sources' locations in water (near its surface) and on the bottom. The case in the presence of ice.

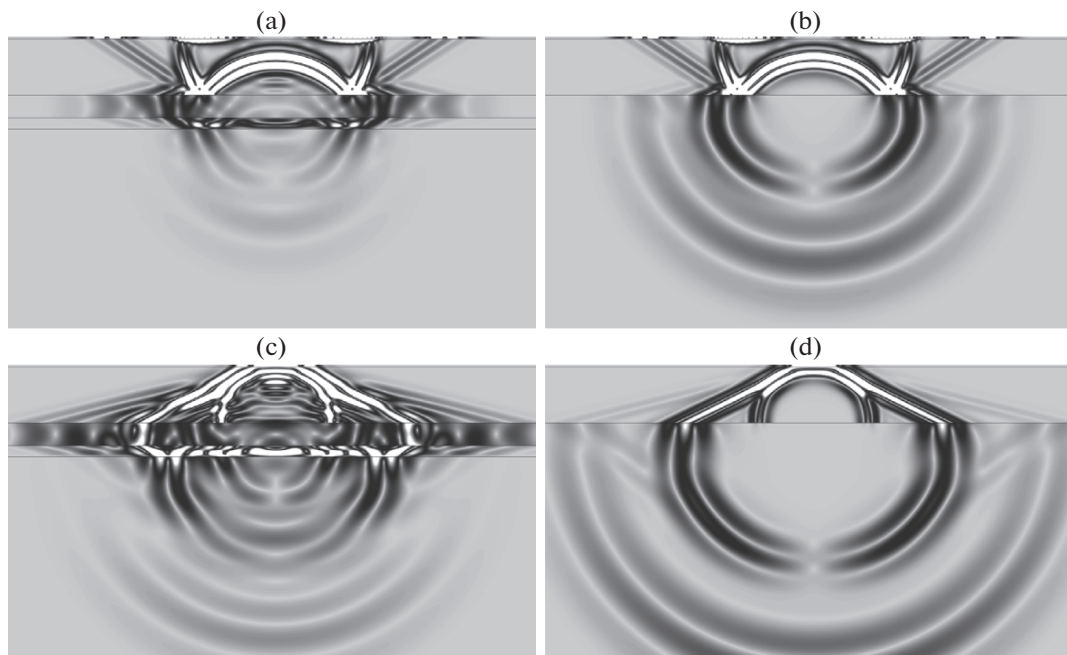


**Fig. 5.** Wave patterns. Comparison between sources' locations in ice and on the bottom. The case in the absence of ice.

Figure 7 presents the wave pattern formed in the iceberg and water at time moment 0.055 s. The velocity modulus is shown in gray and the zone of cracks in the iceberg is shown in black.

### 7. 3D MODELING OF SEISMIC EXPLORATION PROBLEMS IN THE ARCTIC REGION

For modeling seismic processes under the conditions of the Arctic seas in the 3D case, we performed the calculations on a rectangular grid containing  $5.4 \times 10^7$  nodes to study the signal from the single Ricker wavelet source recorded on the ice surface in the multicomponent ice–water–sediment–inclusion

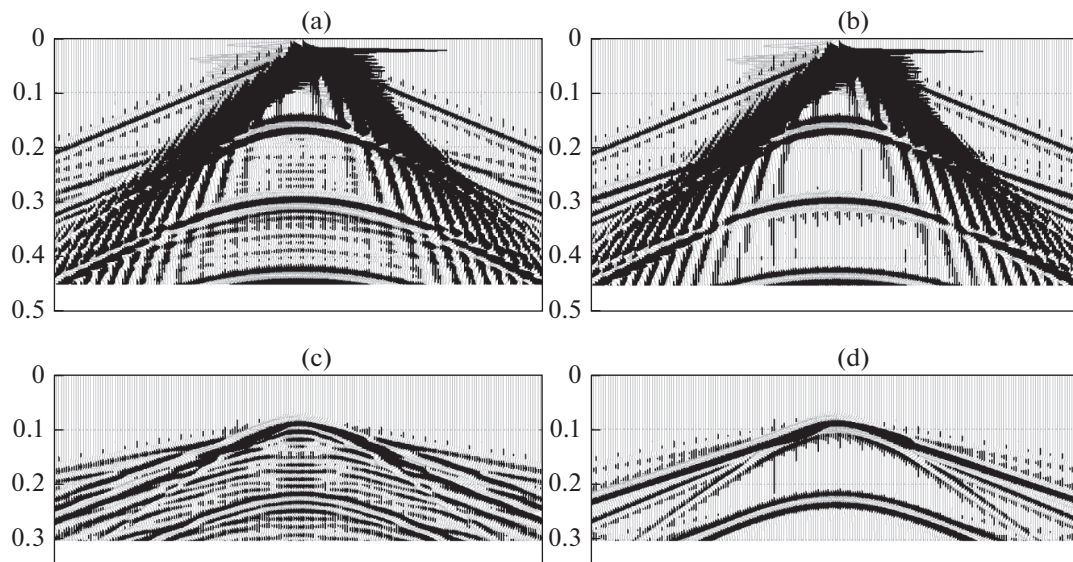


**Fig. 6.** Seismograms (vertical component of velocity). Comparison between sources' locations in ice and on the bottom. The case in the presence of ice.

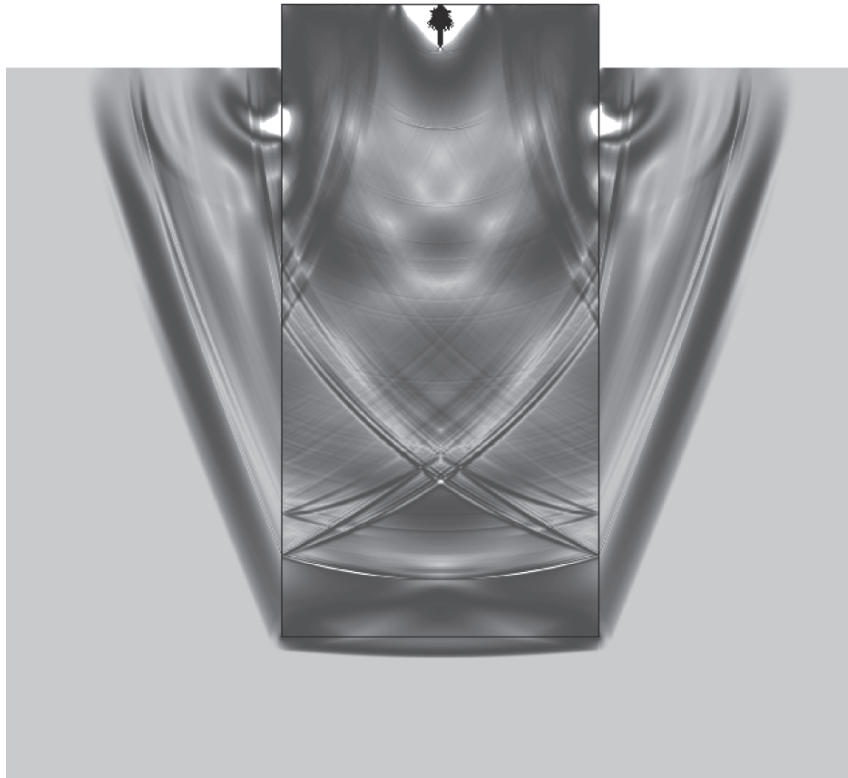


**Fig. 7.** Wave pattern on the effect of the impact on an iceberg and the appearance of a system of cracks. The time moment is 0.055 s.

medium. The width of the integration domain was 120 m and its depth was 60 m. Nonreflecting boundary conditions were set on all sides of the integration domain.

In total, 15000 iterations were made; at every iteration, the time step was  $3 \times 10^{-5}$  s. The step on the coordinate was also constant (0.4 m).

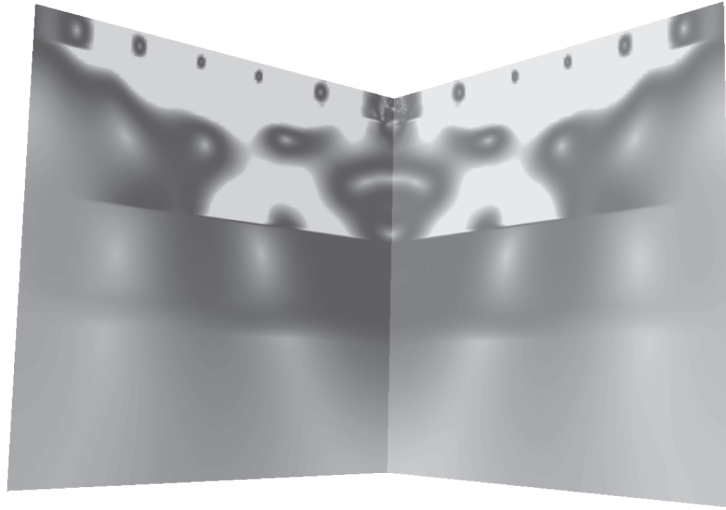


**Fig. 8.** Wave pattern in the ice–water–sediment–inclusion medium.

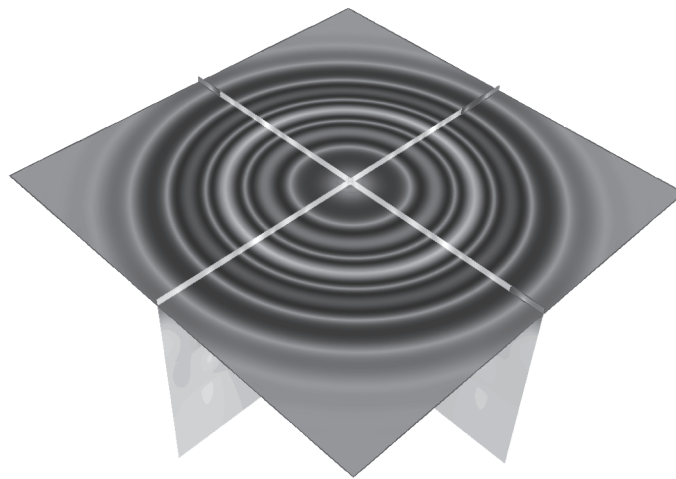


**Fig. 9.** Wave travel in ice.

The following parameters of the medium were assumed: ice thickness of 4 m, ice density of  $917 \text{ kg/m}^3$ ; the  $P$ - and  $S$ -wave velocities were 3940 and 2491 m/s, respectively. The water layer was 20 m thick and  $1000 \text{ kg/m}^3$  in density; the sonic velocity was 1500 m/s. For the sediment having density  $2500 \text{ kg/m}^3$ , the  $P$ - and  $S$ -wave velocities were assumed to be 6500 and 3700 m/s, respectively. The density of the inclusion was assumed to be  $2000 \text{ kg/m}^3$ . The  $P$ - and  $S$ -wave velocities were 4000 and 1250 m/s, respectively.

Figure 8 presents the wave pattern appearing in the integration domain at time moment  $4.510 \times 10^{-4} \text{ s}$ . Figures 9–12 illustrate the sections across the center of the integration domain along two vertical mutually perpendicular planes.

Figures 9–12 also demonstrate horizontal sections in different layers. For example, Fig. 9 shows the propagation of elastic waves in ice at time moment  $4.510 \times 10^{-4} \text{ s}$ . The horizontal section is located at a depth of 2 m from the ice surface.

Figure 10 shows the signal moving through the water. The interference pattern in the center is caused by the interaction between the traveling wave and its reflection from the underlying layers. The section plane is located at a depth of 14 m from the ice surface.

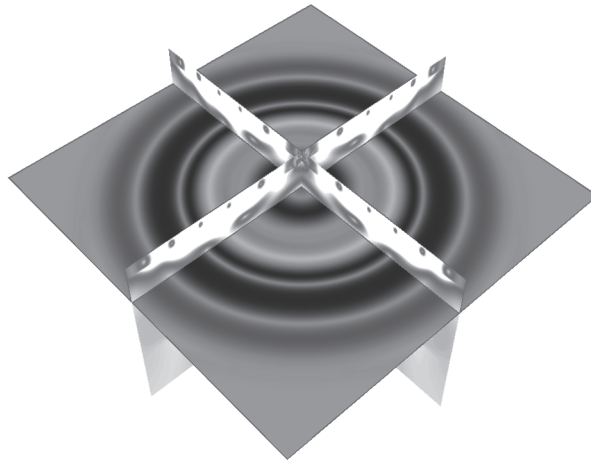


**Fig. 10.** Interference pattern in the water layer.

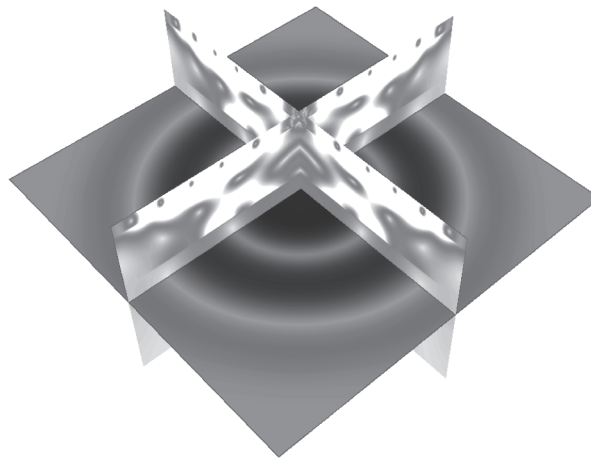


**Fig. 11.** Formation of reflection from the bottom.

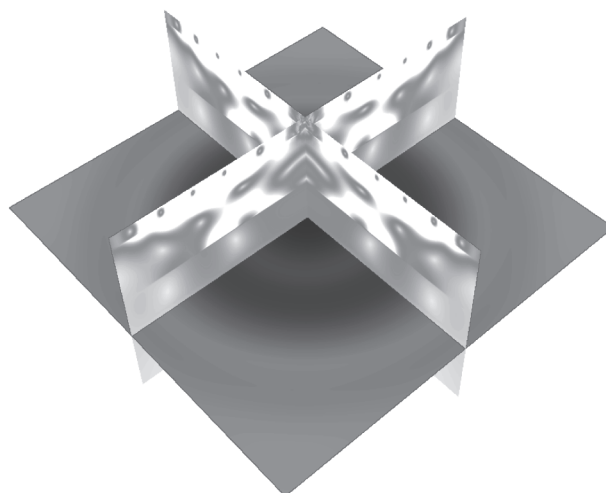


**Fig. 12.** Wave travel through the oil reservoir (inclusion).

The formation of a reflection from the bottom is shown in Fig. 11. The section plane is located at a depth of 30 m from the ice surface. The wave patterns in Figs. 10 and 11 are also at time moment  $4.510 \times 10^{-4}$  s.

The movement of the wave through the oil-containing inclusion is presented in Fig. 12. The horizontal section is at a depth of 38 m from the ice surface.

## 8. CONCLUSIONS

The numerical modeling of wave processes in media with linearly elastic and acoustic layers has been performed. The problems of seismic exploration under the conditions of the Arctic shelf have been solved. Based on the calculations carried out, synthetic seismograms have been constructed; in addition, the effect and mutual influence of ice, the types of set oil reservoirs, and the positions of sources and receivers on the obtained seismograms has been analyzed. The problem on the effect of the impact on an iceberg has also been solved.

## ACKNOWLEDGMENTS

The work was supported by the Ministry of Education and Science of the Russian Federation in the context of subsidy agreement no. 14.575.21.0084 dated October 20, 2014 (the unique ID number of the applied research project is RFMEFI57514X0084).

## REFERENCES

1. Yu. N. Novikov and S. V. Gazhula, "Features of hydrocarbon deposits of the Arctic shelf of Russia evaluation and their revaluation in accordance with the new classification of stocks," *Neftegaz. Geol. Teor. Prakt.*, No. 3, 1–19 (2008).
2. S. G. Lee, S. H. Lun, and G. Y. Kong, "Modeling and simulation system for marine accident cause investigation," in *Collision and Grounding of Ships and Offshore Structure*, Ed. by J. Amdahl, S. Ehlers, and B. J. Leira (CRC, Taylor and France Group, London, 2013).
3. A. T. Bekker, O. A. Sabobash, V. I. Seliverstov, G. I. Koff, and E. N. Pipko, "Estimation of limit ice loads on engineering offshore structures in the See of Okhotsk," in *Proceeding of the 19th International Offshore and Polar Engeneering Conference, 2009*, pp. 574–579.
4. R. V. Gol'dshtein and N. M. Osipenko, "Fracture toughness and ice cover fracture by icebreakers," *Tr. AANII* **391**, 137–156 (1986).
5. R. V. Gol'dshtein and N. M. Osipenko, "Questions of ice and ice cover fracture mechanics in the analysis of ice loads," in *Gas Science News. Modern Approaches and Advanced Technologies in the Projects of Development of Oil and Gas Fields of the Russian Shelf* (Gazprom, VNNIGAZ, Moscow, 2013), No. 3 (4), pp. 104–112 [in Russian].
6. D. G. Levchenko, A. V. Zakirov, and V. D. Levchenko, "Dynamic modeling of the propagation of low-frequency seismic acoustic fields in the oceanic medium," *Dokl. Earth Sci.* **435**, 1623–1626 (2010).
7. V. A. Miryakha, A. V. Sannikov, and I. B. Petrov, "Discontinuous Galerkin method for numerical simulation of dynamic processes in solids," *Math. Models Comput. Simul.* **7**, 446–455 (2015).
8. M. S. Zhdanov, *Geophysical Inverse Theory and Regularization Problems* (Nauchnyi mir, Moscow, 2007), p. 710 [in Russian].
9. W. Nowacki, *Theory of Elasticity* (PWN, Warszawa, 1970; Mir, Moscow, 1975).
10. I. B. Petrov, A. V. Favorskaya, A. V. Sannikov, and I. E. Kvasov, "Grid-characteristic method using high-order interpolation on tetrahedral hierarchical meshes with a multiple time step," *Math. Models Comput. Simul.* **5**, 409–415 (2013).
11. L. D. Landau and E. M. Lifshitz, *Course of Theoretical Physics*, Vol. 6: *Fluid Mechanics* (Nauka, Moscow, 1986; Pergamon, New York, 1987).
12. W. Nowacki, *Wave Problems of Elasticity Theory* (Mir, Moscow, 1978), p. 307 [in Russian].
13. V. I. Golubev, I. B. Petrov, and N. I. Khokhlov, "Numerical simulation of seismic activity by the grid-characteristic method," *Comput. Math. Math. Phys.* **53**, 1523–1533 (2013).
14. A. Harten, "High resolution schemes for hyperbolic conservation laws," *J. Comput. Phys.* **135**, 260–278 (1997).
15. I. B. Petrov and N. I. Khokhlov, "Comparison of TVD limiters for the numerical solution of the deformable solid dynamics equations using the grid-characteristic method," in *Mathematical Models and Problems of Control*, Collection of Articles (2011), pp. 104–111 [in Russian].
16. P. L. Roe, "Characteristic-based schemes for the Euler equations," *Ann. Rev. Fluid Mech.*, No. 18, 337–365 (1986).
17. V. I. Golubev, "Technique of visualization and interpretation of full-wave seismic modeling results," *Tr. MFTI* **6**, 154–161 (2014).